Amine-Functionalized Titanate Nanosheet-Assembled Yolk@Shell Microspheres for Efficient Cocatalyst-Free Visible-Light Photocatalytic CO_2 Reduction

Shengwei Liu,* Jiaqiu Xia, and Jiaguo Yu*

State Key Laboratory of Advanced Technology for Materials Synthesis and Processing, Wuhan University of Technology, Wuhan 430070, P. R. China

S *Supporting Information*

ABSTRACT: Exploiting advanced semiconductor photocatalyst with superior activity and selectivity for the conversion of CO_2 into solar fuels and valuable chemicals is of worldwide interest. In this report, hierarchical amine-functionalized titanate nanosheets based yolk@shell microspheres were synthesized via one-pot organic amine mediated anhydrous alcoholysis of titanium(IV) butoxide. The selected organic amine, diethylenetriamine, played multiple roles. First, it was essential for the crystallographic, morphological and textural control of the synthesized titanate nanoarchitectures. Second, it was crucial for the in situ functionalization of titanate nanosheets by concurrent interlayer intercalation and surface grafting, which gave rise to the strong visible-light absorption ability and high CO_2 adsorption capacity. As a consequence of the synergetic tuning in multilevel microstructures, an integrated engineering of the multifunctional modules of the titanate-based photocatalysts was achieved for efficient CO_2 reduction toward solar fuels.

KEYWORDS: photocatalysis, titanate, nanosheets, amine-functionalized, CO_2 reduction, visible-light
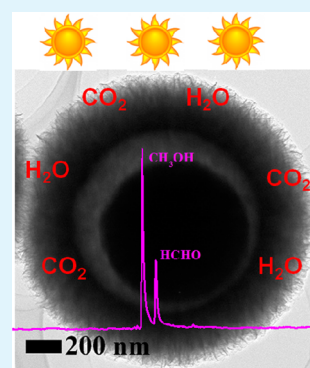
1. INTRODUCTION

The serious worldwide greenhouse effects, disastrous environmental pollution and extremely urgent fossil fuels shortage have led to an increasing interest in developing artificial photosynthesis for producing solar fuels and valuable chemicals.[1−7] Although significant advances have been achieved in the past years, the photocatalytic CO_2 conversion efficiency toward the desired hydrocarbon products is still rather low and is far from stratifying practical applications.[6] Exploiting advanced semiconductor photocatalyst with superior activity and selectivity is urgently desirable but remains as one of the greatest challenges. Titania and a variety of other semiconductor photocatalysts were fabricated and modified by various methods to enhance photocatalytic performances.[3−8]

Inspired by the exceptional properties and great application potentials of graphene, fabrication and application of various two-dimensional (2D) nanosheets other than graphene have attracted tremendous attention.[9−11] Titanate nanomaterials with layered structure, consisting of TiO_6 octahedral layers and interlayer compensating positive ions, have attracted considerable attention because of their excellent physiochemical properties and a wide range of applications, especially in the field of photocatalysis.[12−14] As for promising photocatalysts, the band-edge positions of the layered titanate nanomaterials including the valence band top and the conduction band bottom are located at desirable potential levels.[12,15] The anisotropic layered structure facilitates favorable vectorial separation and transportation of photogenerated charge carriers as well as flexible nanostructural construction with consequence of special size and morphological effects.[9,12] Moreover, the characteristic layered structures of titanate favors the highly tolerable interlayer and surface modification by ion intercalation, organic grafting, and nanoparticle loading, leading to unique multifunctional combination and cooperation.[16−19]

Two basic kinds of strategies have been developed for the fabrication of 2D titanate nanosheets. Conventionally, 2D titanate nanosheets were prepared via top-down strategy involving layer-by-layer exfoliation of a parent layered titanate bulk, typically driven by interlayer intercalation of organic ions (e.g., quaternary ammonium cations).[12] Alternatively, bottom-up strategy based on a simple alkaline hydrothermal method was recently developed for the convenient preparation of 2D titanate nanosheets in high yield.[13] Moreover, the alkaline hydrothermal method facilitated the coupled synthesis and assembly of 2D titanate nanosheets toward higher-level hierarchical architectures with special structural advantages for practical applications.[20−24] However, the as-prepared titanate photocatalysts usually had larger band gap, even compared to titania, and no desirable visible-light absorption was achieved.[13] Besides, creating those titanate architectures typically required inorganic alkaline aqueous solution with ultrahigh concentrations (typically, concentrated NaOH solution in 10 M), which make it difficult to extend the applications of titanate nanomaterials in cost-effective and environmentally benign

manner. It would be very interesting to discover certain mild reaction mediators (other than conventional strong inorganic bases) that can introduce suitable alkaline environment for designable formation of titanate nanostructures,[17] and simultaneously, bring specific guest moieties for interlayer and surface modification giving rise to exceptional optical and surface properties. In this report, organic amine mediated solvothermal alcoholysis of titanium(IV) butoxide in the absence of water was exploited for one-pot constructing titanate hierarchical yolk@shell microspheres. Simultaneously, both interlayer and surface chemistry of the as-prepared titanate samples were modified in situ by selected diethylenetriamine as a typical organic amine. As a consequence, the as-prepared titanate samples exhibited high visible-light harvesting ability, large CO_2 capture capacity and efficient photocatalytic CO_2 reduction performance.

2. EXPERIMENTAL SECTION

2.1. Preparation. All chemicals were analytical grade and used without further purification. The hierarchical titanate yolk@shell microspheres were synthesized referencing the previously published procedures,[25−27] but paying special attention at avoiding water being involved in the whole synthesis processes because the presence of water will change the crystallographic phase and morphology of resulting products. In a typical synthesis, 0.1 mL of diethylenetriamine (DETA) was first added to 80 mL of isopropyl alcohol under vigorous stirring, and then (5 min later) 3 mL of titanium(IV) butoxide was added, and the mixed solution was sealed and stirred constantly for another 10 min. Subsequently, the mixture was transferred into a 200 mL Teflon-lined autoclave and kept in an electric oven at 200 °C for 24 h. The yellow precipitates were harvested via centrifugation, washed thoroughly with ethanol and water, and dried at 80 °C overnight. The obtained sample was denoted as TN200. For comparison, sample was also prepared in the absence of DETA under otherwise identical conditions and the corresponding sample was denoted as T200. In addition, the effects of solvothermal temperatures (160 and 180 °C) and time (2, 6, 12, 36, and 72 h) and additional calcination treatment at higher temperature (300, 400, and 500 °C) on the structures and/or properties of the synthesized samples were also investigated. The calcination was proceeded in air for 1h and the ramping rate was set at 3 °C min^{-1}. The sample names and the corresponding synthesis conditions are listed in Table S1 in the Supporting Information.

2.2. Characterization. X-ray diffraction (XRD) patterns obtained on a D/Max-RB X-ray diffractometer (Rigaku, Japan) with Cu Kα irradiation at a scanning rate of 0.05° 2θ s^{-1} were used to determine the phase structures of the samples. Field-emission scanning electron microscopy (FESEM) images were examined by an S-4800 (Hitachi, Japan) scanning electron microscope. Transmission electron microscopy (TEM) and high-resolution transmission electron microscopy (HRTEM) analyses were performed on a JEM-2100F electron microscope (JEOL, Japan) using a 200 kV accelerating voltage. Nitrogen sorption isotherms were measured on an ASAP 2020 gas adsorption apparatus (Micromeritics, USA). All the samples were degassed at 180 °C prior to nitrogen sorption measurements. The Brunauer−Emmett−Teller (BET) surface area was determined by a multipoint BET method, using the adsorption data in the relative pressure (P/P_0) range of 0.05−0.3. The adsorption branch of nitrogen sorption isotherms was used to determine the pore size distribution by the Barret-Joyner-Halender (BJH) method, assuming a cylindrical pore model.[28] The volume of nitrogen adsorbed at the relative pressure (P/P_0) of 0.97 was used to determine the pore volume and the average pore size. CO_2 adsorption was measured using an ASAP 3020 carbon dioxide adsorption apparatus (Micromeritics, USA). UV−visible diffuse reflectance spectra of the samples were obtained on a UV-2550 UV−visible spectrophotometer (Shimadzu, Japan). A fine BaSO$_4$ power was used as a reflectance standard in a UV−vis diffuse reflectance experiments. Fourier transform infrared (FTIR) spectra of the samples were recorded using an IR Affinity-1 FTIR spectrometer

(Shimadzu, Japan). X-ray photoelectron spectroscopy (XPS) measurements were carried out using an ultrahigh vacuum VG ESCALAB 210 electron spectrometer using Mg Kα radiation. XPS data were calibrated using the binding energy of C 1s (284.8 eV) as the internal standard. Fourier transform (FT) Raman spectra were recorded on a Nexus FT infrared spectrometer (Thermo Nicolet, USA) equipped with a Raman module accessory using a Nd^{3+}:YVO$_4$ laser (1064 nm) as the near-infrared excitation source. Zeta potential was analyzed using the MPT-2 Multi-Purpose Titrator linked with a Zetasizer Nano instrument (Malvern, USA).

2.3. Photocatalytic Reduction of CO_2. The photocatalytic reduction of CO_2 was operated in a 200 mL homemade Pyrex reactor at ambient temperature and atmospheric pressure, similar to our previously reported procedures.[29,30] Typically, 100 mg of catalyst was suspended into 10 mL of DI water in a glass reactor via ultrasonic dispersion for 30 min, and then dried at 80 °C over 2 h. The catalysts were deposited onto the bottom of the reactor forming a thin and smooth film. Before light irradiation, the reactor was sealed and deoxidized by blowing nitrogen for 30 min to remove air. CO_2 and H_2O vapor were produced from the reaction of NaHCO$_3$ (0.12 g, introduced into the reactor before seal) and HCl aqueous solution (0.25 mL, 4 M), which was injected into the reactor via a syringe. A 300W Xe arc lamp (Changzhou Siyu Science Co. Ltd., China) with a UV-cutoff filter ($\lambda \geq 400$ nm) was used as a light source and positioned ∼22 cm above the photocatalytic reactor. The focused intensity measured using a visible-light radiometer (Model: FZ-A, China) was ca. 150 W cm^{-2}. The gas product taken from the reactor was analyzed using a gas chromatograph (GC-2014C, Shimadzu) equipped with a flame ionized detector (FID) and methanizer. Product gases were calibrated with a standard gas mixture and determined using the retention time. Each photocatalytic CO_2 reduction cycle in this study was performed in triplicates.

3. RESULTS AND DISCUSSION

3.1. Crystallographic Structures. The crystallographic structures of the as-synthesized products were studied by XRD and Raman analyses. As shown in Figure S1A (Supporting Information), only two recognizable diffraction peaks located around $2\theta = 25$ and $48°$ was recorded for the sample TN200, and the XRD diffraction peaks were very weak and wide, suggesting the smaller crystallite size and/or poor crystallinity of the present solvothermally synthesized samples. Note that, similar synthesis procedures were employed in previous studies to fabricate titania nanostructures with additional calcination treatment, and those two diffraction peaks was assigned to anatase (101) and (200) planes.[25] In fact, it was hard to identify the crystallographic phase based only on these two XRD diffraction peaks. In this situation, the Raman spectroscopy as a more sensitive method was carried out to further clarify the crystallographic structures. Note that because of the low degree of crystallinity and strong photoluminescence interference, no resolvable Raman peak was recorded for TN200 using visible-light laser (514.5 nm Ar$^+$ laser) as excitation source (Figure S2A in the Supporting Information). To exclude the shielding effects of photoluminescence, Fourier transform (FT) Raman spectrum using 1064 nm near-infrared excitation source (Nd^{3+}:YO$_4$ laser) was recorded, as shown in Figure 1. The spectrum presented weak and broad Raman vibrational peaks centered around 197, 276, 386, 446, 672, 702, 786, 822, and 926 cm^{-1}, which can not be assigned to either anatase or rutile TiO_2, but shared similar peak positions and profiles to the layered lepidocrocite titanate nanostructures with a typical chemical formula, $H_xTi_{2-x/4}\square_{x/4}O_4$ ($\square$: vacancy).[31−34] In this regard, the aforementioned two XRD diffraction peaks located around $2\theta = 25$ and $48°$ were related to protonated titanate (110) and (200) planes, respectively.[31] The added DETA as a
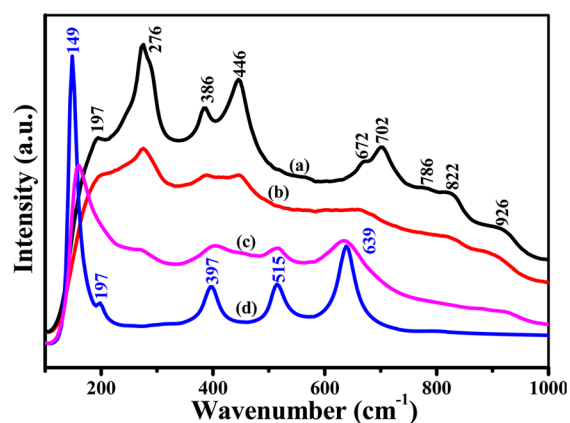
Figure 1. Fourier transform (FT) Raman spectra of (a) TN200 in comparison with (b) TN160, (c) T200, and (d) TN200−500 using 1064 nm near-infrared excitation source (Nd³⁺:YO₄ laser).

typical organic amine with strong basicity in the solvothermal synthesis system was crucial for the formation of the as-obtained titanate products.[17] The samples prepared without the DETA under otherwise identical conditions (denoted as T200 in Table 1 and Table S1 in the Supporting Information) was well-crystallized as anatase TiO_2 (JCPDS card no. 21−1272; space group $I4_1/amd$ (141); $a_0 = 3.7852$ Å, $c_0 = 9.5139$ Å), as evidenced by XRD (Figure S1 in the Supporting Information) and Raman (Figure 1) analyses.

Notably, the synthesis conditions, including the solvothermal temperature and time, were also important for the controlled synthesis of titanate products. No samples were obtained when the solvothermal temperature was below 160 °C, whereas dark colored samples can be readily produced with solvothermal temperature above 160 °C. The samples obtained at different solvothermal temperature (below 200 °C as we used) shared the similar crystallographic structures but with perceptible difference in the degree of crystallinity, as evidenced by varied Raman peak intensity for TN160 versus TN200 (Figure 1). Obviously, higher solvothermal temperature corresponded to titanate sample with higher degree of crystallinity. As expected, the degree of crystallinity of the samples can also be largely modified by the solvothermal treatment time (Figure S1B and Figure S2 in the Supporting Information). Moreover, phase transition from titanate to anatase titania occurred during the solvothermal treatment after progressively extending the solvothermal treatment time up to 36 and 72 h (Figure S1B and Figure S2 in the Supporting Information). Overall, during solvothermal treatment processes, two phase transformation processes occurred, that is, conversion of amorphous titanate to progressively crystallized titanate and subsequent conversion of titanate to anatase titania. By simple calcination, the solvothermally synthesized titanate products can also be easily transformed into well crystallized anatase TiO_2 (Figure S1C in the Supporting Information and Figure 1). Note that the slight

change in the Raman peak positions for sample T200 versus TN200−500 was probably resulted from their different crystallite size and morphology.

3.2. Morphological Aspects. Similar to reported results,[25−27] the DETA mediated anhydrous alcoholysis of titanium(IV) butoxide under one-pot solvothermal conditions (above 160 °C) generally gave rise to hierarchical titanate microspheres with typical yolk@shell configuration, as indicated by FESEM and TEM images for sample TN200 (Figure 2a−c, see a detailed morphological depiction in the
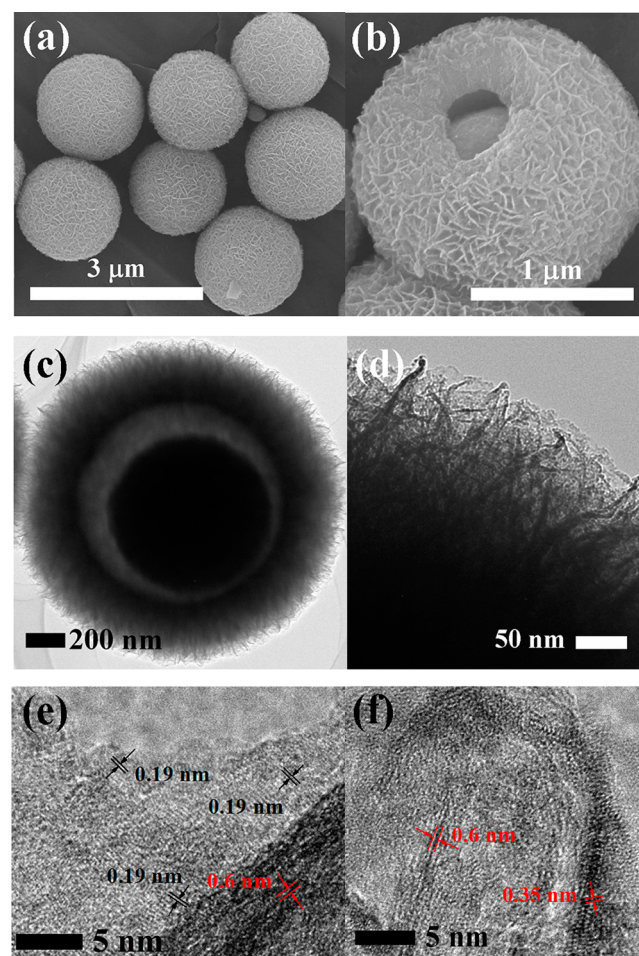

Figure 2. (a, b) FESEM, (c, d) TEM, and (e, f) HRTEM images of the typical sample TN200.

Supporting Information). It was expected that such yolk@shell structures should introduce multireflections of incident light within the hollow chamber and improve the light harvesting, which was beneficial for photocatalytic applications.[26] The combined SEM and TEM observation reflected that the yolk was aggregate of tiny nanoparticles, whereas the shell was built

Table 1. Basic Physicochemical Properties and Photocatalytic Performance of the Typical Samples

sample	S_{BET} (m²g⁻¹)	pore volume (cm³g⁻¹)	average pore size (nm)	N/Ti ratio	CO_2 adsorption (mmol g⁻¹)	CH_3OH production rate (μmol h⁻¹g⁻¹)
TN160	465	0.28	2.4	0.35	1.34	0.8
TN200	246	0.18	3.0	0.31	0.79	2.1
TN200−500	91	0.3	13.1	0.03	0.11	0
T200	107	0.12	4.45	0	0.45	0.3

by irregular assembly of nanosheets. The nanosheets on the external surface of the shell were so thin that they were transparent and curved in the enlarged TEM image (Figure 2d). The nanosheets were interwoven and gave rise to highly porous framework. The high-resolution TEM (HRTEM) image (Figure 2e, f) indicated that the nanosheets may be lying parallel or standing perpendicular to the grid surface. The lying nanosheets indicted that the thin TiO_2 nanosheets (Figure 2e) were not single-crystalline but were further assembled by tiny nanosheets via oriented attachment, as illustrated by the isolated visible lattice fringes sharing the similar orientation on a single nanosheet. The distance of the observed lattice fringes was measured to be close to 0.19 nm, corresponding to the interplane spacing of (200) facets of hydrogen titanate.[17] The standing nanosheets (Figure 2e, f) reflected the thickness of the nanosheets varying in the range of 2−5 nm, the interplane distance of about 0.35 nm was related to (110) facets, and the interplane distance of about 0.6 nm was related to interlayer spacing of titanate nanosheets along *b* axis ([010] direction).[17,31−34] The reflected crystallographic microstructure was consistent with the aforementioned Raman analysis, corresponding to the layered orthorhombic lepidocrocite hydrogen titanate.[17,31−34]

The formation processes the as-prepared uniform hierarchical titanate yolk@shell microspheres conformed well to our previously proposed chemically induced self-assembly and in situ self-transformation (CIST) mechanism,[35,36] based on the time-dependent evolution experiments and systematic XRD (Figure S1B in the Supporting Information), SEM and TEM investigations (Figure S3 in the Supporting Information). Notably, the added DETA in the present study was necessary for the formation of the uniform hierarchical titanate yolk@shell microspheres, controlling both the crystallographic and morphological evolution. Without DETA, both the self-assembly process to amorphous spherical framework and their consequent self-transformation process toward crystalline titanate yolk@shell counterparts was out of control, and thus, only ill-shaped anatase titania microspheres was formed with relatively smooth surface (Figure S4 in the Supporting Information).

The multilevel microstructures of the synthesized titanate products could be easily tuned by a variety of synthesis parameters, including solvothermal temperature, concentration of added DETA as well as the organic amine selected. For example, the solvothermal temperature affected both the alcoholysis dynamics of titanium(IV) butoxide and the rate of dissolution and recrystallization process, as a consequence, the solvothermal temperature affected both the size and morphology of the synthesized titanate spheres (Figure S5 in the Supporting Information). The average diameter of the synthesized titanate spheres was reduced from 1.8 μm to 600 and 400 nm as the solvothermal temperature was reduced from 200 to 180 and 160 °C, respectively. Moreover, as the solvothermal temperature was reduced to 160 °C, no visible nanosheets was formed on the external surface of the synthesized TN160 titanate spheres. Upon calcination, the hierarchical titanate yolk@shell microspheres converted into well-crystallized anatase TiO_2 counterparts with remaining yolk@shell morphology, but the sphere size was greatly reduced to 1.2 μm.

3.3. Pore Structures. To characterize the specific surface area and porosity of the as-prepared hierarchical titanate yolk@shell microspheres, we carried out N_2 sorption analysis. Figure

3 showed the N_2 sorption isotherms and the corresponding pore size distribution curves of the sample TN200 in
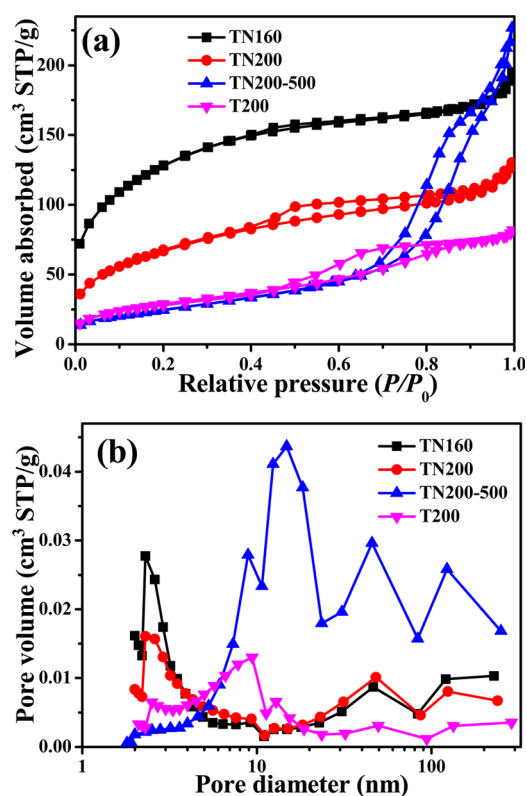

Figure 3. (a) Nitrogen adsorption−desorption isotherms and (b) the corresponding pore size distribution curves for sample TN200 in comparison with TN160, T200 and TN200−500.

comparison with other related reference samples. The nitrogen sorption isotherm (Figure 3a) of sample TN200 was a combination of types I and IV (BDDT classification).[28] At a low relative pressure range (below 0.4), the isotherm exhibited a high adsorption associated with the presence of micropores (type I), suggesting that the samples still contained a large portion of amorphous titanate (in good agreement with weak and wide peak in the corresponding XRD result).[37] At higher relative pressures, the isotherm exhibited an interconnected hysteresis loop associated with capillary condensation of gases within mesopores. Significantly, the hysteresis loop covered a broad range of relative pressures from approximately 0.4 to 1.0, consistent with the wide mesopore size distribution within the as-prepared hierarchical titanate yolk@shell microspheres. In addition, the lack of plateau on the adsorption isotherm at the relative pressures approaching 1 indicated the presence of macropores.[38] This wide pore size distribution was further confirmed by the corresponding pore size distribution curves (Figure 3b). Interestingly, the as-prepared hierarchical titanate yolk@shell microspheres contained micropores (below 2 nm), small mesopores (from 2 to 10 nm), large mesopores (from 10 to 50 nm) and macropores (above 50 nm), which demonstrated the existence of multilevel nanoporous structures resulted from the hierarchical assembly of the basic building blocks including both tiny 0D nanoparticles and 2D nanosheets. The BET surface area (S_{BET}) and pore volume of the as-prepared hierarchical titanate yolk@shell microspheres was 246 m^2 g^{-1} and 0.18 cm^3 g^{-1}, respectively (Table 1). By contrast,

the sample TN160 prepared at lower solvothermal temperature basically had similar hierarchical pore structures as that of the sample TN200, but it had larger S_{BET} (465 m^2 g^{-1}) and pore volume (0.28 cm^3 g^{-1}). It was believed that such a highly porous framework within the as-prepared yolk@shell structured hierarchical titanate microspheres would be beneficial for enhancing molecular adsorption and diffusion during photocatalytic reactions.

It has been demonstrated above that DETA was crucial for regulating the assembly and transformation processes during the formation of as-prepared hierarchical titanate yolk@shell microspheres. In this connection, the added DETA was also important for the formation of the aforementioned multilevel nanoporous structures. As the N$_2$ sorption isotherm of sample T200 shown in Figure 3a, the adsorption in low relative pressure range (below 0.45) was obviously reduced, consistent with the good crystallization of sample T200 with much lower micropores. The hysteresis loop associated with mesopores by intra- and interaggregation was located within narrower relative pressures(from 0.45 to 0.9), which was consistent with the uniform particle size and morphology of the building blocks (just 0D nanoparticles), giving rise to narrower pore size distribution (Figure 3b). In addition, the adsorption related to macropores at the relative pressures approaching 1 decreased, suggesting that less macropores was formed within T200 microspheres. Overall, as shown in Figure 3b, the micropores and macropores were not favored in the absence of DETA, and the resulting pore sized distribution within T200 microspheres was much narrower, with a dominant monomodel mesopores size distribution centered around 10 nm. Relatively, the sample T200 prepared without DETA had smaller S_{BET} (107 m^{2}g^{-1}) and pore volume (0.12 cm^{3}g^{-1}) (Table 1) as compared with the sample TN200 counterpart.

Upon calcination, although the resulting TiO$_2$ products (TN200−500) basically remained in the hierarchical yolk@shell morphology (Figure S6 in the Supporting Information), great changes occurred in pore structures. Both the micropores and small mesopores almost vanished, accompanied by the right shift of the hysteresis loop toward higher relative pressure ranges (from 0.65 to 1), as a consequence of the enhanced crystallization and ripening of crystallite, giving rise to larger aggregation-induced mesopores. Moreover, great increase occurred in adsorption related to macropores at the relative pressures approaching 1. Interestingly, after calcination, the pore volume was largely increased from 0.18 to 0.3 cm^{3}g^{-1}, in contrast to the great reduce in S_{BET} from 246 to 91 m^2 g^{-1} (Table 1). The reduce in S_{BET} was resulted from growth in crystallite size, whereas the increase in pore volume originated from the removal of organic moieties.

3.4. Guest Modification (Surface Grafting). In addition to the mediating effects over the crystallographic, morphological, and porous structures, the added DETA may also greatly modify the synthesized titanate host by guest incorporation involving either interlayer intercalation or surface grafting. The chemical components of the sample TN200 were investigated by XPS analysis in comparison with the samples TN160, T200, and TN200−500. On the basis of the survey spectra (Figure S7a in the Supporting Information), in addition to the dominant Ti and O peaks, two obvious peaks related to C and N species were detected in the sample TN200. To determine the nature of guest moieties present in the titanate host, the high-resolution XPS spectra of N 1s and C 1s core level were examined, as shown in Figure 4. The chemical nature
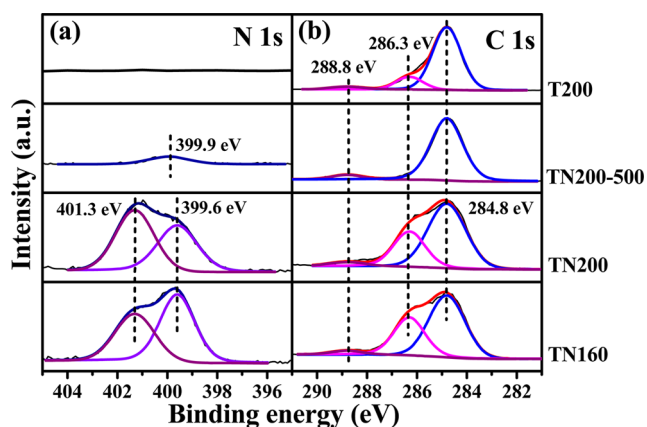
Figure 4. High-resolution XPS spectra of (a) N 1s and (b) C 1s for sample TN200 in comparison with TN160, T200, and TN200−500.

of the N species in N-modified TiO$_2$ was a major point under debate, depending on the specific synthesis processes.[39] Taking account of the employed mild solvothermal conditions in the present study, the incorporated azo moieties shall mainly modified the surface and interlayer space of titanate host, instead of entering into the TiO$_6$ octahedral layers. As expected, N 1s peak associated with substitutional N with a binding energy of 396−397 eV was not detected. The high resolution XPS spectrum of N 1s for TN200 can be well deconvoluted into two peaks (Figure 4a). The peak located at the lower binding energy (centered at 399.6 eV) can be assigned to surface grafted amine (−NH$_2$), while the another peak located at the higher binding energy (centered at 401.3 eV) can be attributed to protonated amine (−NH$_3^+$) intercalated between TiO$_6$ octahedral layers.[17] Obviously, the incorporated N-species were originated from the added DETA, as shown in Figure 4a, no N signal was detected for the sample T200 prepared without DETA. Note that, the solvothermal temperature affected the loading amount and states of incorporated N-species. The N/Ti ratio was 0.35 and 0.31 for TN160 and TN200, respectively (Table 1). Moreover, higher solvothermal temperature favored more −NH$_3^+$ intercalated into the interlayer space between the TiO$_6$ octahedral layers of titanate host. However, after calcination at 500 °C in air for 1 h, the titanate was converted into anatase titania, and the layered structures were completely destroyed, as a result, the intercalated −NH$_3^+$ was readily removed from the calcined sample TN200−500, surprisingly, a small portion of surface grafted −NH$_2$ was not eliminated but transformed into substitutional NH$_x$ and NO$_x$ in the titania host.[39]

The XPS spectrum of C 1s (Figure 4b) for TN200 can be fitted into three peaks at 284.8, 286.3, and 288 eV, which were assigned to carbon atoms in the C−C, C−O, and C═O bonds, respectively.[40] Similarly, no C 1s peak for Ti−C bonds (around 281 eV) resulted from the substitution of O with C in TiO$_6$ octahedra was recorded, suggesting that carbon also mainly modified on the surface and/or interlayer of sample TN200. Although the three C peaks can be observed in all the solvothermally synthesized samples (TN160, TN200, and T200), obviously, as shown in Figure 4b, the added DETA favored the surface modification with carbonaceous moieties via C−O−Ti bonds. After calcination at 500 °C in air for 1 h, only two peaks corresponding to C−C and C═O bonds were left for sample TN200−500, whereas the C 1s peak related to C−O bonds vanished. Upon high-temperature calcination up to 500

°C, the surface carbonaceous modifier shall be mostly removed, as supported by the TG-DTA analysis (Figure S8 in the Supporting Information); therefore, it was believed that most of the recorded C−C and C═O peaks for sample TN200−500 were mainly originated from surface adsorbed hydrocarbon and CO_2 from air as adventitious contaminant. The grafting amount of C- and N-containing organic moieties on the surface and interlayer of sample TN200 was estimated to be about 19 wt % (Figure S8 in the Supporting Information). Unfortunately, although the IR absorption associated with vibration of C−C, C−H, and C−O bonding was recorded, the surface grafted −NH$_2$ and −NH$_3^+$ can not be exclusively identified by FTIR spectroscopy (Figure S9 in the Supporting Information), because of the sensitivity limit and possible peak overlapping.

3.5. Light Absorption. It has been well-demonstrated that enhanced visible-light photocatalytic efficiency of TiO_2 could be readily achieved by introducing various dopants (especially, nonmetal species) into the TiO_2 host, which gave rise to various localized states within the bandgap and/or grafted chromophoric complexes as sensitizer on the surface.[39] Figure 5
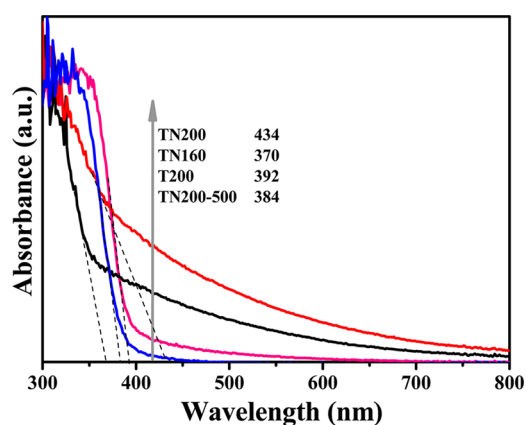

Figure 5. UV−vis diffuse reflection spectra of sample TN200 in comparison with TN160, T200, and TN200−500. The inset showed the absorption edges.

showed the UV−visible diffuse reflectance spectra for sample TN200 together with other related references. The sample TN200 showed strong visible-light absorption in wide region from 400 nm up to 800 nm, with the absorption edge at the 434 nm. Obviously, both the absorption range and the characteristic absorption edge of sample TN200 were tuned[12,20] by the grafted C and N species on the surface or interlayer of titanate host, which would probably act as both visible-light sensitizer and bandgap engineer. Relative to TN200, the sample TN160 showed significantly less redshift in the absorption edge (370 nm) and slightly weaker absorption in visible-light region. Taking account of the weaker interlayer −NH$_3^+$ intercalation in TN160 versus TN200 (Figure 4), it seemed that the interlayer intercalated −NH$_3^+$ was much important in narrowing the band gap of titanate. In contrast, although the sample T200 contained a large portion of surface modified C−O moieties, it showed a very limited visible-light absorption above 400 nm with the absorption edge at 392 nm. In this regard, it was supposed that grafted N-containing species on the surface or interlayer of as-prepared titanate contributed more for the wide and strong visible-light absorption. As a confirmation, after calcination of TN200 at 500 °C in air, most surface-grafted N-containing species was removed, and the

resulting sample TN200−500 also showed very limited visible-light absorption above 400 nm with the absorption edge shifting to 384 nm. The bandgap energies (Figure S10 in the Supporting Information) were roughly estimated to be about 3.35, 2.65, 3.15, and 3.20 eV for the samples TN160, TN200, T200, and TN200−500, respectively.

Note that the long-tail absorption in the visible-light region (400−800 nm) may be attributed to surface defects.[39,41,42] Calcination of TN200 at 300 °C leading to strongest visible light absorption (Figure S10 in the Supporting Information) was just because of the introduction of higher density of defects during removal of grafted C/N-species.[41] Higher-temperature calcination of TN200 at 500 °C in air reduced not only the surface grafting level but also the defect density.[41] The phase transformation from modified layered titanate to clean titania, with higher crystallization and higher packing density of TiO$_6$ octahedra, resulted in lower tolerance to dopants and defects and loss of visible-light absorption ability (Figure S10 in the Supporting Information). The solvothermal temperature and subsequent calcination temperature affected the grafting process and grafting level, as well as the complementary defects, which together affected the visible-light harvesting capacity of the related samples (Figure S10 in the Supporting Infomration).

3.6. CO$_2$ Adsorption. Besides the influence over light absorption, the surface modification with C and N species affected a variety of the surface physicochemical properties, including surface basicity and charge (Figure S11 in the Supporting Information), which greatly affected the CO_2 adsorption performance on the synthesized hierarchical titanate yolk@shell microspheres. The adsorption of CO_2 onto the photocatalyst surface was the first essential step affecting the reaction pathway and dynamics of the photocatalytic CO_2 reduction.[4,5] We investigated the CO_2 adsorption performance of sample TN200 in comparison with sample TN160, T200, and TN200−500 using CO_2 adsorption isotherms. As shown in Figure 6, the sample TN200 exhibited a rapid rise in CO_2
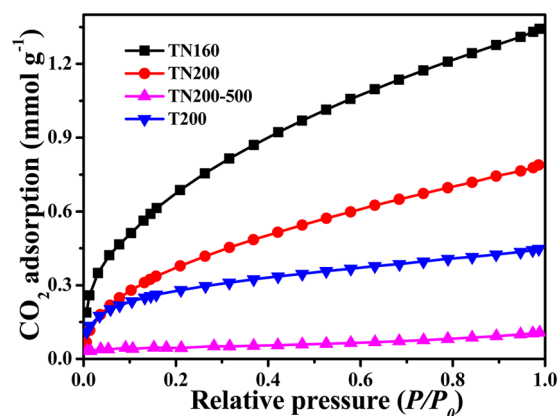

Figure 6. CO_2 adsorption isotherms of sample TN200 in comparison with TN160, T200, and TN200−500.

uptake along with elevated CO_2 pressure at a relatively low level ($P/P_0 < 0.2$), as a consequence of specific interactions between CO_2 and the surface organic grafters including hydroxyl and amine groups.[30] Meanwhile, the sample TN200 had high specific surface area and pore volume, endowing it with high CO_2 uptake ability at higher P/P_0 conditions ($P/P_0 > 0.2$).[30] More CO_2 could be adsorbed within the hierarchical

nanopores of the yolk@shell microspheres. Because of larger surface grafting level of organic amine and higher specific surface area (Table 1), the sample TN160 had an even larger CO_2 adsorption capacity. However, the sample T200 prepared without DETA shown much lower CO_2 adsorption capacity as compared with TN200, highlighting the crucial role of DETA in modifying the surface properties and pore structure for CO_2 capture. As expected, the sample TN200−500 showed greatly reduced CO_2 adsorption capacity, as a consequence of reduced specific surface area and limited active adsorption sites after the removal of organic grafters by calcination treatment.

3.7. Photocatalytic Activity. Photocatalytic CO_2 reduction activity was evaluated using the synthesized various samples under visible-light irradiation ($\lambda \geq 400$ nm). Figure 7a showed the original chromatogram for the photocatalytic
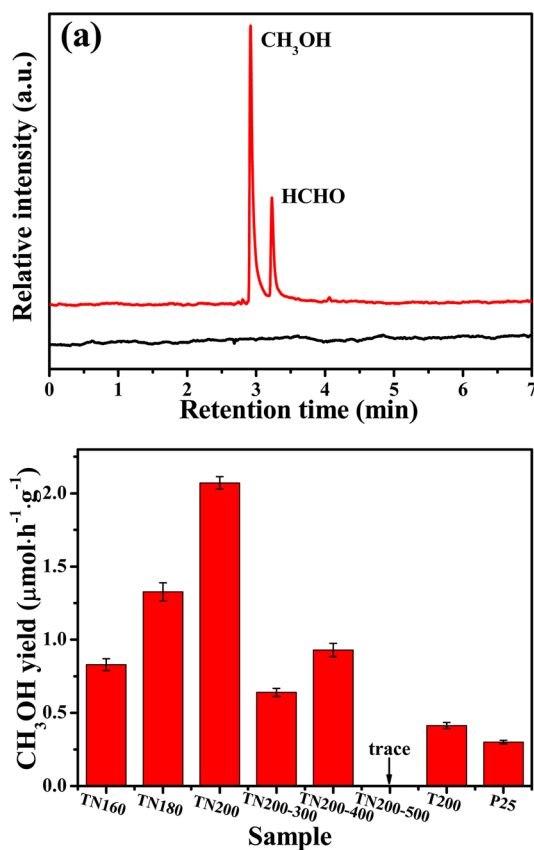

Figure 7. (a) Original chromatograms for sample TN200 after 1 h irradiation in contrast to that without catalyst or light irradiation and (b) comparison of CH_3OH generation rate for various typical samples.

reduction of CO_2 over sample TN200. CH_3OH was yielded as the major product, with a small amount of HCHO. Control experiments indicated that no appreciable reduction products were detected in the absence of either photocatalyst or light irradiation, suggesting that the CO_2 reduction was proceeded via photocatalytic reaction on the photocatalyst. The photocatalytic CO_2 reduction process and mechanism was quite complex. In principle, the proton-assisted multielectron CO_2 reduction pathway, involving electron and proton transfer, C−O bond breaking, C−H/C−C bond formation, was thermodynamically more favorable than the one-electron CO_2 reduction pathway.[2−4] Taking account of the reduction products detected in the present study, the typical two-electron, two-proton reaction pathway involving formaldehyde

as characteristic intermediate was proposed.[2] Note that the CH_4, a common product using various TiO_2 photocatalysts,[29,30] was not detected in the present study. It seemed the surface amine functionalization can not account for the product selectivity,[43] the combined contribution from the titanate with higher conduction band level and interlayer amine functionalization in tuning the reaction pathway and products shall be further investigated.

Figure 7b showed the comparison of visible-light photocatalytic production rates of CH_3OH over samples synthesized under different conditions and Degussa P 25. Overall, the sample TN200 showed the best activity in photocatalytic CO_2 reduction toward generation of CH_3OH as valuable solar fuel. The combined special crystallographic and surface properties of TN200 were responsible for its superior photocatalytic CO_2 reduction performance. As compared with titania, the layered framework of titanate with lower packing density endowed it with higher interlayer and surface loading ability toward organic grafters, acting as both light-harvesting centers and active adsorption centers. The resulting both higher visible-light-harvesting ability and larger CO_2 adsorption capacity contributed to higher photocatalytic CO_2 reduction activity. The post calcination treatment of TN200 induced the transformation of titanate to titania as well as the removal of grafted organic moieties, and generally reduced the photocatalytic CO_2 reduction activity (Figure 7b and Table 1). Moreover, it was generally documented that, as compared with titania, the titanate was much inactive for photocatalytic reactions in terms of hydrogen production and organics oxidation,[14] which were harmful back or side reactions for photocatalytic CO_2 reduction toward solar fuels, including CH_3OH.[4] This assumption was also supported by our preliminary results. Although no hydrogen was detected during photocatalytic CO_2 reduction using TN200 as photocatalyst, detectable chromatogram peaks for hydrogen was recorded using the sample T200 (2 μmol h^{-1} g^{-1}) and TN200−500 (8 μmol h^{-1} g^{-1}) as photocatalyst. Meanwhile, the photocatalytic oxidation ability toward mineralization of organics, as a back reaction against CO_2 reduction, was largely enhanced after conversion of TN200 to titania by high-temperature calcination, evidenced using RhB as an example (Figure S12 in the Supporting Information).[26] Overall, as a result of limited visible-light absorption ability, inferior CO_2 adsorption capacity, and serious back reactions, both sample T200 and calcined samples, especially TN200−500, showed very limited photocatalytic CO_2 reduction activity toward CH_3OH production. By the way, as the titania conduction band potential is just close to the CO_2 and water reduction potential, cocatalyst is usually necessary to reduce overpotential for efficient photocatalytic CO_2 reduction,[44] and thus, in the present study, cocatalyst-free photocatalytic CO_2 reduction is much lower using titania as photocatalyst.

With increasing solvothermal temperature from 160 to 200 °C, the CH_3OH production rate increased greatly from 0.8 to 2.1 μmol h^{-1} g^{-1} (Figure 7 and Table S1 in the Supporting Information). The solvothermal temperature largely affected the various structural and chemical parameters, including the morphological and textural characteristics, degree of crystallinty and defect density, as well as the chemical composition in terms of NH_2/NH_3^+ content and ratio, water content, etc. All those differences were possibly responsible for the difference in light-harvesting ability, CO_2 adsorption capacity, and photocatalytic CO_2 reduction activities. For example,

although the higher specific surface area and higher loading amount of surface organic grafter for TN160 endowed it with higher CO_2 adsorption capacity, the weaker visible-light-harvesting ability (Figure 5) and inferior degree of crystallinity (Figure 1and Figure S1 in the Supporting Information) for TN160 made it with relatively inefficient charge generation and transportation toward surface catalytically active sites for photocatalytic CO_2 reduction. On the other hand, the suitable solvothermal time is also important in tuning the CH_3OH production rate. As the solvothermal temperature was set at 200 °C, the CH_3OH production rate first increased with increasing solvothermal time up to 24 h, and then reduced with further increasing solvothermal time to 36 and 72 h (Figure S13 and Table S1 in the Supporting Information). The crystallographic characteristics (including crystal polymorph and crystallinity), textural features (including morphology and pore structures), and interlayer and surface guest incorporation (affecting light harvesting and reactant adsorption) was varied, which was crucial in tuning the photocatalytic CO_2 reduction properties. The photocatalytic stability of sample TN200 was studied as a typical example. The time-dependent CH_3OH yield did not linearly increase with prolonged light irradiation time (Figure S14A in the Supporting Information). In fact, this was similar to the case for many reported photocatalysts.[2] After more than 3 h, the increase in CH_3OH yield was almost suspended for TN200. However, if the photocatalysts were recollected and washed after each service and reused again for the 1 h photocatalytic CO_2 reduction cycle, the stability was not bad, and the activity was reduced by about 10% after six cycles (Figure S14B in the Supporting Information). In this regard, it was believed that some organic products adsorbed on the photocatalysts surface and inhibited the continuous activity in photocatalytic CO_2 reduction.

It is generally recognized that four interconnected basic processes are involved for various photocatalytic redox reactions (including photocatalytic CO_2 reduction) over TiO_2 or other photocatalysts, that is, first light absorption and excitation to produce photogenerated charge carriers (holes and electrons), then charge separation and bulk transport toward the catalyst surface, subsequently, reactant adsorption and activation by interfacial charge transfer from catalyst surface to adsorbed reactants, and finally, the surface redox reactions with targeted pathway and kinetics.[4] Accordingly, the photocatalytic material systems dominating the photocatalytic processes can be divided into four functional modules, that is, light-active centers, charge transportation channel, adsorption centers and the catalysis-active centers. In this sense, modifying photocatalytic processes and performances could be primarily achieved by designing the related functional modules, which are essentially dependent on engineering the multilevel structures, including electronic, crystallographic, surface, and textural structures of the employed photocatalyst. An integrated engineering of the multilevel structures would enable a synergetic tuning of the four functional modules, a comprehensive optimization of the overall interconnected complex photocatalytic processes and a maximum enhancement of the photocatalytic efficiency. The constructed titanate nanosheet-assembled hierarchical yolk@shell microspheres in this study is just a model example, in which the integrated engineering of multilevel microstructures was one-pot achieved for the synergetic tuning of the four functional modules and thus the great enhancement in photocatalytic performances. The added DETA is crucial, enabling the integrated engineering

of multilevel microstructures and the multifunctional modules of the photocatalytic material systems. First, the DETA facilitated the formation of titanate as dominant crystallographic phase by providing suitable alkaline reaction environment. Generally, titanate has a favorable band structure with a higher conduction band than that of titania,[15] which is thermodynamically desirable for photocatalytic CO_2 reduction even without the assistance of cocatalyst.[4] Moreover, the anisotropic layered crystallographic structure of titanate itself and the incurring favored formation of ultrathin sheetlike titanate nanostructures together facilitate favorable vectorial separation and transportation of photogenerated charge carriers.[9] In addition, the layered structure facilitates either the interlayer or surface guest incorporation,[16−19] as a result, both the electronic structures and surface properties were modified to enhance both light harvesting and CO_2 capture. Second, the added DETA affects the self-assembly and self-transformation processes toward constructing titanate nanosheets-assembled yolk@shell microspheres, giving rise to unique structural advantages as well as accompanying hierarchical porosity and higher specific surface area, all contributing to enhanced light harvesting and CO_2 capture. Third, the added DETA acts as sources of the guest modifier, which contributes to both interlayer and surface grafting of C- and N-containing moieties. Overall, all four functional modules are modified simultaneously by the one-pot DETA-mediated programmed design of crystallographic, textural (both morphological and porous), electronic, and surface properties; as a consequence, the photocatalytic processes and performance are well integratively tuned to great extent.

4. CONCLUSIONS

Visible-light-responsive nanosheet-assembled hierarchical titanate yolk@shell microspheres with engineered multilevel microstructures and efficient photocatalytic CO_2 reduction performance were synthesized via DETA-mediated anhydrous alcoholysis of titanium(IV) butoxide under one-pot solvothermal conditions. The formation the hierarchical titanate yolk@shell microspheres conformed to the typical chemically induced self-assembly and in situ self-transformation mechanism, and the selected DETA was crucial in directing morphological and crystallographic evolution as well as the formation of hierarchical porous structures. Simultaneously, the visible-light absorption ability and the CO_2 adsorption capacity would be tuned by the DETA involved interlayer and surface modification of the titanate host. As a result of synergetic tuning of the multifunctional modules of the photocatalytic system, especially light-harvesting centers and CO_2 adsorption centers, the designed amine-functionalized titanate yolk@shell microspheres can be used as efficient photocatalysts for cocatalyst-free photocatalytic reduction of CO_2 to dominant CH_3OH. The present study would inspire new ideas in designing advanced photocatalysts with delicate multifunctional modules to control the photocatalytic processes and to enhance the photocatalytic performances by integrated engineering of the multilevel structures.

■ ASSOCIATED CONTENT

Ⓢ Supporting Information

We provide preparation conditions for various samples and additional XRD patterns, Raman spectra, SEM and TEM images, XPS spectra, TG-DTA curves, FT-IR spectrum, UV−vis diffuse reflection spectra and band gap analysis, zeta

potential analysis, photocatalytic RhB oxidation degradation and photocatalytic CH_3OH production activities, and stability of some reference samples. This material is available free of charge via the Internet at http://pubs.acs.org/.

■ AUTHOR INFORMATION

Corresponding Authors
*E-mail:sliu@whut.edu.cn.
*E-mail: jiaguoyu@yahoo.com. Tel.: 0086-27-87871029. Fax: 0086-27-87879468.

Notes
The authors declare no competing financial interest.

■ ACKNOWLEDGMENTS

■ REFERENCES

(1) Inoue, T.; Fujishima, A.; Konishi, S.; Honda, K. Photo-electrocatalytic Reduction of Carbon Dioxide in Aqueous Suspensions of Semiconductor Powders. *Nature* **1979**, *277*, 637−638.

(2) Habisreutinger, S. N.; Schmidt-Mende, L.; Stolarczyk, J. K. Photocatalytic Reduction of CO_2 on TiO_2 and Other Semiconductors. *Angew. Chem., Int. Ed.* **2013**, *52*, 7372−7408.

(3) Ma, Y.; Wang, X. L.; Jia, Y. S.; Chen, X. B.; Han, H. X.; Li, C. Titanium Dioxide-Based Nanomaterials for Photocatalytic Fuel Generations. *Chem. Rev.* **2014**, *114*, 9987−10043.

(4) Li, X.; Wen, J. Q.; Low, J. X.; Fang, Y. P.; Yu, J. G. Design and Fabrication of Semiconductor Photocatalyst for Photocatalytic Reduction of CO_2 to Solar Fuel. *Sci. China Mater.* **2014**, *57*, 70−100.

(5) Marszewski, M.; Cao, S. W.; Yu, J. G.; Jaroniec, M. Semiconductor-Based Photocatalytic CO_2 Conversion. *Mater. Horiz.* **2015**, DOI: 10.1039/C4MH00176A.

(6) Roy, S. C.; Varghese, O. K.; Paulose, M.; Grimes, C. A. Toward Solar Fuels: Photocatalytic Conversion of Carbon Dioxide to Hydrocarbons. *ACS Nano* **2010**, *4*, 1259−1278.

(7) Tu, W. G.; Zhou, Y.; Zou, Z. G. Photocatalytic Conversion of CO_2 into Renewable Hydrocarbon Fuels: State-of-the-Art Accomplishment, Challenges, and Prospects. *Adv. Mater.* **2014**, *26*, 4607−4626.

(8) Zhou, P.; Yu, J. G.; Jaroniec, M. All-Solid-State Z-Scheme Photocatalytic Systems. *Adv. Mater.* **2014**, *26*, 4920−4935.

(9) Zhou, M.; Lou, X. W.; Xie, Y. Two-Dimensional Nanosheets for Photoelectrochemical Water Splitting: Possibilities and Opportunities. *Nano Today.* **2013**, *8*, 598−618.

(10) Low, J. X.; Cao, S. W.; Yu, J. G.; Wageh, S. Two-Dimensional Layered Composite Photocatalysts. *Chem. Commun.* **2014**, *50*, 10768−10777.

(11) Cao, S. W.; Yu, J. G. g-C_3N_4-Based Photocatalysts for Hydrogen Generation. *J. Phys. Chem. Lett.* **2014**, *5*, 2101−2107.

(12) Wang, L. Z.; Sasaki, T. Titanium Oxide Nanosheets: Graphene Analogues with Versatile Functionalities. *Chem. Rev.* **2014**, *114*, 9455−9486.

(13) Bavykin, D. V.; Friedrich, J. M.; Walsh, F. C. Protonated Titanatesand TiO_2 Nanostructured Materials: Synthesis, Properties, and Applications. *Adv. Mater.* **2006**, *18*, 2807−2824.

(14) Yu, J. G.; Yu, H. G.; Cheng, B.; Trapalis, C. Effects of Calcination Temperature on the Microstructures and Photocatalytic Activity of Titanate Nanotubes. *J. Mol. Catal. A-Chem.* **2006**, *249*, 135−142.

(15) Li, X. K.; Kikugawa, N.; Ye, J. H. Nitrogen-doped Lamellar Niobic Acid with Visible Light-responsive Photocatalytic Activity. *Adv. Mater.* **2008**, *20*, 3816−3819.

(16) Sun, X. M.; Li, Y. D. Synthesis and Characterization of Ion-Exchangeable Titanate Nanotubes. *Chem.—Eur. J.* **2003**, *9*, 2229−2238.

(17) Dinh, C. T.; Seo, Y. B.; Nguyen, T. D.; Kleitz, F.; Do, T. O. Controlled Synthesis of Titanate Nanodisks as Versatile Building Blocks for the Design of Hybrid Nanostructures. *Angew. Chem., Int. Ed.* **2012**, *51*, 6608−6612.

(18) Kim, T. W.; Hwang, S. J.; Jhung, S. H.; Chang, J. S.; Park, H.; Choi, W.; Choy, J. H. Bifunctional Heterogeneous Catalysts for Selective Epoxidation and Visible Light Driven Photolysis: Nickel Oxide-Containing Porous Nanocomposite. *Adv. Mater.* **2008**, *20*, 539−542.

(19) Ide, Y.; Matsuoka, M.; Ogawa, M. Efficient Visible-Light-Induced Photocatalytic Activity on Gold-Nanoparticle-Supported Layered Titanate. *J. Am. Chem. Soc.* **2010**, *132*, 16762−16764.

(20) Feng, M.; You, W.; Wu, Z. S.; Chen, Q. D.; Zhan, H. B. Mildly Alkaline Preparation and Methylene Blue Adsorption Capacity of Hierarchical Flower-like Sodium Titanate. *ACS Appl. Mater. Interfaces.* **2013**, *5*, 12654−12662.

(21) Cao, L.; Chen, D. H.; Caruso, R. A. Surface-Metastable Phase-Initiated Seeding and Ostwald Ripening: A Facile Fluorine-Free Process towards Spherical Fluffy Core/Shell, Yolk/Shell, and Hollow Anatase Nanostructures. *Angew. Chem.* **2013**, *125*, 11192−11197.

(22) Tang, Y. F.; Yang, L.; Chen, J. Z.; Qiu, Z. Facile Fabrication of Hierarchical Hollow Microspheres Assembled by Titanate Nanotubes. *Langmuir* **2010**, *26*, 10111−10114.

(23) Yu, J. G.; Li, Q. L.; Fan, J. J.; Cheng, B. Fabrication and Photovoltaic Performance of Hierarchically Titanate Tubular Structures Self-assembled by Nanotubes and Nanosheets. *Chem. Commun.* **2011**, *47*, 9161−9163.

(24) Li, W.; Deng, Y. H.; Wu, Z. X.; Qian, X. F.; Yang, J. P.; Gu, D.; Zhang, F.; Tu, B.; Zhao, D. Y. Hydrothermal Etching Assisted Crystallization: A Facile Route to Functional Yolk-Shell Titanate Microspheres with Ultrathin Nanosheets-Assembled Double Shells. *J. Am. Chem. Soc.* **2011**, *133*, 15830−15833.

(25) Chen, J. S.; Tan, Y. L.; Li, C. M.; Cheah, Y. L.; Luan, D. Y.; Madhavi, S.; Boey, F. Y. C.; Archer, L. A.; Lou, X. W. Constructing Hierarchical Spheres from Large Ultrathin Anatase TiO_2 Nanosheets with Nearly 100% Exposed (001) Facets for Fast Reversible Lithium Storage. *J. Am. Chem. Soc.* **2010**, *132*, 6124−6130.

(26) Fang, W. Q.; Yang, X. H.; Zhu, H. J.; Li, Z.; Zhao, H. J.; Yao, X. D.; Yang, H. G. Yolk@Shell Anatase TiO_2 Hierarchical Microspheres with Exposed {001} Facets for High-Performance Dye Sensitized Solar Cells. *J. Mater. Chem.* **2012**, *22*, 22082−22089.

(27) Li, Z. T.; Ren, Z. Y.; Qu, Y.; Du, S. C.; Wu, J.; Kong, L. J.; Tian, G. H.; Zhou, W.; Fu, H. G. Hierarchical N-Doped TiO_2 Microspheres with Exposed (001) Facets for Enhanced Visible Light Catalysis. *Eur. J. Inorg. Chem.* **2014**, 2146−2152.

(28) Sing, K. S. W.; Everett, D. H.; Haul, R. A. W.; Moscou, L.; Pierotti, R. A.; Rouquerol, J.; Siemieniewska, T. Reporting Physisorption Data for Gas/Solid Systems with Special Reference to the Determination of Surface Area and Porosity (Recommendations 1984). *Pure Appl. Chem.* **1985**, *57*, 603−619.

(29) Yu, J. G.; Low, J. X.; Xiao, W.; Zhou, P.; Jaroniec, M. Enhanced Photocatalytic CO_2-Reduction Activity of Anatase TiO_2 by Coexposed {001} and {101} Facets. *J. Am. Chem. Soc.* **2014**, *136*, 8839−8842.

(30) Fu, J. W.; Cao, S. W.; Yu, J. G.; Low, J. X.; Lei, Y. P. Enhanced Photocatalytic CO_2-Reduction Activity of Electrospun Mesoporous TiO_2 Nanofibers by Solvothermal Treatment. *Dalton Trans.* **2014**, *43*, 9158−9165.

(31) Mao, Y. B.; Wong, S. S. Size- and Shape-Dependent Transformation of Nanosized Titanate into Analogous Anatase Titania Nanostructures. *J. Am. Chem. Soc.* **2006**, *128*, 8217−8226.

(32) Qian, L.; Du, Z. L.; Yang, S. Y.; Jin, Z. S. Raman Study of Titania Nanotube by Soft Chemical Process. *J. Mol. Struct.* **2005**, *749*, 103−107.

(33) Liu, H. W.; Zheng, Z. F.; Yang, D. J.; Waclawik, E.; Ke, X. B.; Zhu, H. Y.; Palmer, S.; Frost, R. L. A Raman Spectroscopic Study on the Allocation of Ammonium Adsorbing Sites on $H_2Ti_3O_7$ Nanofibre and Its Structural Derivation During Calcination. *J. Raman Spectrosc.* **2010**, *41*, 1601−1605.

(34) Hu, W. B.; Li, L. P.; Li, G. S.; Liu, Y.; Withers, R. L. Atomic-scale Control of TiO_6 Octahedra through Solution Chemistry towards Giant Dielectric Response. *Sci. Rep.* **2014**, *4*, 6582 (1−9).

(35) Liu, S. W.; Yu, J. G.; Cheng, B.; Jaroniec, M. Fluorinated Semiconductor Photocatalysts: Tunable Synthesis and Unique Properties. *Adv. Colloid Interface Sci.* **2012**, *173*, 35−53.

(36) Liu, S. W.; Huang, G. C.; Yu, J. G.; Ng, T. W.; Yip, H. Y.; Wong, P. K. Porous Fluorinated SnO_2 Hollow Nanospheres: Transformative Self-assembly and Photocatalytic Inactivation of Bacteria. *ACS Appl. Mater. Interfaces* **2014**, *6*, 2407−2414.

(37) Yu, J. G.; Liu, W.; Yu, H. G. A One-Pot Approach to Hierarchically Nanoporous Titania Hollow Microspheres with High Photocatalytic Activity. *Cryst. Growth Des.* **2008**, *8*, 930−934.

(38) Yu, X. X.; Yu, J. G.; Cheng, B.; Jaroniec, M. Synthesis of Hierarchical Flower-like AlOOH and TiO_2/AlOOH Superstructures and their Enhanced Photocatalytic Properties. *J. Phys. Chem. C* **2009**, *113*, 17527−17535.

(39) Asahi, R.; Morikawa, T.; Irie, H.; Ohwaki, T. Nitrogen-Doped Titanium Dioxide as Visible-Light-Sensitive Photocatalyst: Designs, Developments, and Prospects. *Chem. Rev.* **2014**, *114*, 9824−9852.

(40) Zhao, L.; Chen, X. F.; Wang, X. C.; Zhang, Y. J.; Wei, W.; Sun, Y. H.; Antonietti, M.; Titirici, M. M. One-Step Solvothermal Synthesis of a Carbon@TiO_2 Dyade Structure Effectively Promoting Visible-Light Photocatalysis. *Adv. Mater.* **2010**, *22*, 3317−3321.

(41) Liu, S. W.; Yu, J. G.; Wang, W. G. Effects of Annealing on the Microstructures and Photoactivity of Fluorinated N-doped TiO_2. *Phys. Chem. Chem. Phys.* **2010**, *12*, 12308−12315.

(42) Yu, J. G.; Li, Q.; Liu, S. W.; Jaroniec, M. Ionic-Liquid-Assisted Synthesis of Uniform Fluorinated B/C-Codoped TiO_2 Nanocrystals and Their Enhanced Visible-Light Photocatalytic Activity. *Chem.—Eur. J.* **2013**, *19*, 2433−2441.

(43) Liao, Y. S.; Cao, S. W.; Yuan, Y. P.; Gu, Q.; Zhang, Z. Y.; Xue, C. Efficient CO_2 Capture and Photoreduction by Amine-Functionalized TiO_2. *Chem.—Eur. J.* **2014**, *20*, 10220−10222.

(44) Varghese, O. K.; Paulose, M.; LaTempa, T. J.; Grimes, C. A. High-Rate Solar Photocatalytic Conversion of CO_2 and Water Vapor to Hydrocarbon Fuels. *Nano Lett.* **2009**, *9*, 731−737.